*J. Fluid Mech.* (2016), *vol.* 786, *pp.* 5–28. © Cambridge University Press 2015
doi:10.1017/jfm.2015.634



# Experimental study of rotating-disk boundary-layer flow with surface roughness

**Shintaro Imayama[1], P. Henrik Alfredsson[1] and R. J. Lingwood[1,2,†]**

[1]Linné Flow Centre, KTH Mechanics, SE-100 44 Stockholm, Sweden

[2]Centre for Simulation and Applied Mechanics, School of Engineering and Materials Science, Queen Mary University of London, Mile End Road, London E1 4NS, UK

(Received 15 January 2015; revised 9 July 2015; accepted 24 October 2015;
first published online 24 November 2015)

Rotating-disk boundary-layer flow is known to be locally absolutely unstable at $R > 507$ as shown by Lingwood (*J. Fluid Mech.*, vol. 299, 1995, pp. 17–33) and, for the clean-disk condition, experimental observations show that the onset of transition is highly reproducible at that Reynolds number. However, experiments also show convectively unstable stationary vortices due to cross-flow instability triggered by unavoidable surface roughness of the disk. We show that if the surface is sufficiently rough, laminar–turbulent transition can occur via a convectively unstable route ahead of the onset of absolute instability. In the present work we compare the laminar–turbulent transition processes with and without artificial surface roughnesses. The differences are clearly captured in the spectra of velocity time series. With the artificial surface roughness elements, the stationary-disturbance component is dominant in the spectra, whereas both stationary and travelling components are represented in spectra for the clean-disk condition. The wall-normal profile of the disturbance velocity for the travelling mode observed for a clean disk is in excellent agreement with the critical absolute instability eigenfunction from local theory; the wall-normal stationary-disturbance profile, by contrast, is distinct and the experimentally measured profile matches the stationary convective instability eigenfunction. The results from the clean-disk condition are compared with theoretical studies of global behaviours in spatially developing flow and found to be in good qualitative agreement. The details of stationary disturbances are also discussed and it is shown that the radial growth rate is in excellent agreement with linear stability theory. Finally, large stationary structures in the breakdown region are described.

**Key words:** absolute/convective instability, nonlinear instability, transition to turbulence

## 1. Introduction

The exact similarity solution of the governing equations for the laminar flow induced by the rotation of a disk of infinite radius was derived by von Kármán (1921). Figure 1 in Imayama, Alfredsson & Lingwood (2014) shows typical examples of laminar velocity profiles from rotating-disk boundary-layer flow. Here, quantities $U^*$, $V^*$, $W^*$, $r^*$, $z^*$, $\theta$ and the non-dimensional quantities, $U$, $V$, $W$, $R$, $z$ are defined as

† Email address for correspondence: lingwood@mech.kth.se

in Imayama *et al.* (2014), where $*$ denotes a dimensional value. The inflection point of the radial velocity profile makes the flow inviscidly unstable, so-called cross-flow (or Type-I) instability. Since the three-dimensional laminar boundary-layer flow is similar to the swept-wing boundary layer flow, rotating-disk flow is often used as a model for investigation of the laminar transition of swept-wing boundary-layer flows, e.g. Gregory, Stuart & Walker (1955) and Saric, Reed & White (2003).

Linear stability analysis (e.g. Malik, Wilkinson & Orszag 1981) shows inviscidly unstable (Type-I) stationary and travelling disturbances, and the critical Reynolds number of the stationary mode is $R = 287$. Here, as is usual, the definition of Reynolds number in this study is given as the non-dimensional radius, $R = r^*\sqrt{\Omega^*/\nu^*}$, where $r^*$ is local radius, $\Omega^*$ is rotational speed and $\nu^*$ is kinematic viscosity. Although the viscous unstable mode (Type-II) has significantly lower critical Reynolds number at $R = 69.4$ for travelling disturbances with a wave angle of $-19.0°$ (Faller 1991), the spatial growth rate is lower than for the Type-I unstable mode. The highest spatial growth is a Type-I mode that travels significantly more slowly than the rotating disk (Hussain, Garrett & Stephen 2011). However, the Type-I stationary unstable mode is typically observed in experiments as the dominant structure since surface roughnesses excite stationary disturbances continuously in the flow field, whereas the travelling disturbances are not excited continuously without introducing an artificial source of disturbance. Faller (1991) showed theoretically and experimentally that transition to turbulence at lower Reynolds number via a Type-II instability mechanism is possible if the amplitude of the external turbulence disturbance is high enough to excite the Type-II unstable mode.

Although early studies were mainly focused on Type-I stationary instability and the associated laminar–turbulent transition mechanism, Lingwood (1995, 1997) found that some convectively unstable travelling disturbances become locally absolutely unstable above the critical Reynolds number, $R_{CA} = 507.3$, and she suggested that the local absolute instability triggers the onset of transition. Past studies have shown that despite the local absolute instability the rotating-disk flow is linearly globally stable (Davies & Carpenter 2003), results that were supported by the experiments of Othman & Corke (2006). However, more recent work using the linearized complex Ginzburg–Landau equation has shown that the flow could be linearly globally unstable (Healey 2010) if a finite disk radius is taken into account. These findings are supported by linear and nonlinear DNS of rotating-disk flows with a finite linear region, which also show linear and nonlinear global instability provided that the end of the linear region is sufficiently far from $R_{CA}$ (Appelquist *et al.* 2015). Pier (2003) has theoretically shown that above $R_{CA}$ rotating-disk flow is nonlinearly globally unstable, presenting a so-called 'elephant global mode'.

Many experimental studies of rotating-disk flow have been performed, and while some link the onset of nonlinearity in the transition process to the onset of absolute instability, no direct evidence of the absolute instability has been shown except by the propagation of a wavepacket in an impulsively excited rotating-disk boundary-layer flow (Lingwood 1996). However, a recent experimental study by Imayama *et al.* (2014) of 'unexcited' rotating-disk flow (i.e. without artificial excitation) captured two peaks in the spectra in the transitional regime: one identified as due to stationary disturbances and one due to travelling disturbances. Furthermore, using a well-polished glass disk, i.e. a clean-disk condition, Imayama *et al.* (2014) showed that the breakdown of individual stationary vortices is independent of their amplitude and seems to be fixed by the Reynolds number. Experimentally, it is very hard to eliminate Type-I stationary disturbances completely because even if the disk

surface is well polished, unavoidable surface roughnesses continuously excite the stationary disturbances (see Saric *et al.* (2003) for a general discussion on roughness effects in three-dimensional laminar boundary layers). Thus, it is hypothesized that the convectively unstable transition route due to stationary disturbances, i.e. the rough-disk condition, and the absolutely unstable transition route, i.e. the clean-disk condition, compete with each other and depend on the level of surface roughness. Some attempts to clarify the situation have been made by Corke and co-workers at University of Notre Dame, USA. By introducing stationary disturbances via regularly spaced roughness elements on the disk surface (Corke & Knasiak 1998; Corke & Matlis 2006; Corke, Matlis & Othman 2007), they investigated the interaction between stationary and travelling disturbances. They proposed that a triad resonance involving stationary and travelling disturbances is an important mechanism involved in the transition to turbulence and the creation of large-scale structures (low wavenumber modes) in the transitional region.

The present work investigates instability of the boundary-layer flow, also using roughness elements on the disk surface. By changing the number of roughness elements, i.e. leaving parts of the disk free from roughnesses, the laminar–turbulent transition with roughness elements can be directly compared with that occurring for the clean-disk condition. The aim is to add to the understanding of competing laminar–turbulent transition mechanisms for rotating-disk boundary-layer flow. The characteristics of the travelling disturbances captured for the clean-disk condition are further elaborated by comparing with eigenfunctions from linear stability theory, and the front dynamics at the boundary of local convective and absolute instabilities are discussed and compared with early studies. Finally, the large stationary structures appearing in the breakdown regime are discussed and compared with early studies.

## 2. Experimental set-up

The detailed experimental set-up is described in Imayama, Alfredsson & Lingwood (2012, 2013, 2014), see figure 1 in Imayama *et al.* (2012), and only a short description of the set-up is given here. The disk is made from float glass and has a diameter and thickness of 474 mm and 24 mm, respectively. However, the actual radius of the disk was 235.5 mm since the edge of the disk was ground down with a 45° chamfer. The surface of the disk was polished, resulting in a surface roughness of less than 1 μm, and the maximum imbalance was less than 10 μm. The glass disk was mounted horizontally on top of an aluminium-alloy disk and these were connected to a vertical shaft of a d.c. servo motor. The measurements were performed using a single hot-wire probe positioned with a computer-controlled traversing system having two degrees of freedom (radial and vertical directions) that was mounted above the disk and outside the disk edge. The hot-wire sensor had a diameter of 5 μm and a length of 1 mm and the probe was connected to a constant-temperature anemometer (CTA).

The surface roughness elements are intended to excite Type-I stationary cross-flow instability in the flow field. Some earlier studies, e.g. Wilkinson & Malik (1983, 1985) and Corke & Knasiak (1998), performed experiments using roughness elements. Wilkinson & Malik (1983, 1985) used one 0.64 mm square element with a height of 0.13 mm, whereas Corke & Knasiak (1998) used ink-dot patterns as the roughnesses with each dot having a diameter of 1.6 mm and height of 0.06 mm. In this study, dry transfer lettering provided by Letraset® (Letraset Ref. 13045) was used to create each roughness element. Each element is circular and the diameter is approximately

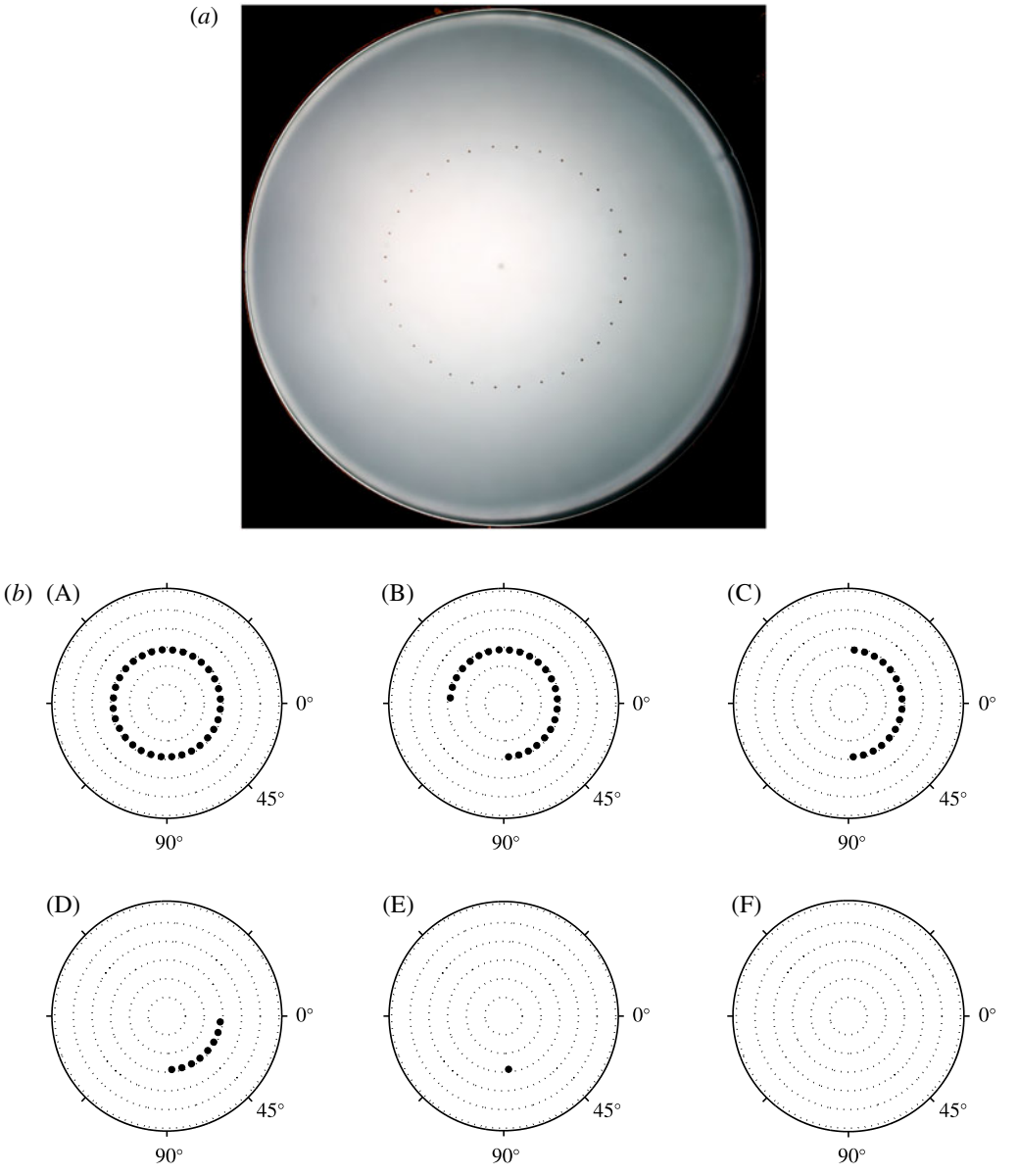


FIGURE 1. (*a*) Top view of the glass-disk surface showing the 32 roughness elements [1–32]. The roughnesses were put at $r^* = 110 \pm 0.5$ mm, corresponding to approximately $R = 287$ in the present study. (*b*) Illustrations of roughness configurations: (A) 32 roughnesses [1–32], (B) 24 roughnesses [1–8, 17–32], (C) 16 roughnesses [1–8, 25–32], (D) 8 roughnesses [1–8], (E) 1 roughness [8], (F) 0 roughnesses (clean-disk condition). The black dots indicate roughness locations (the size is not actual scale). The dashed lines indicate $R = 100$, 200, 300, 400, 500, 600, respectively moving outward. The edge of the disk is shown as an outer solid circle.

2 mm. 32 roughness elements were put at $r^* = 110 \pm 0.5$ mm, corresponding to about $R = 287$ in this study, at angular intervals of $11.25 \pm 0.4°$; see figure 1(*a*). The roughness height was measured by a laser distance meter (opto NCDT 1700-10),

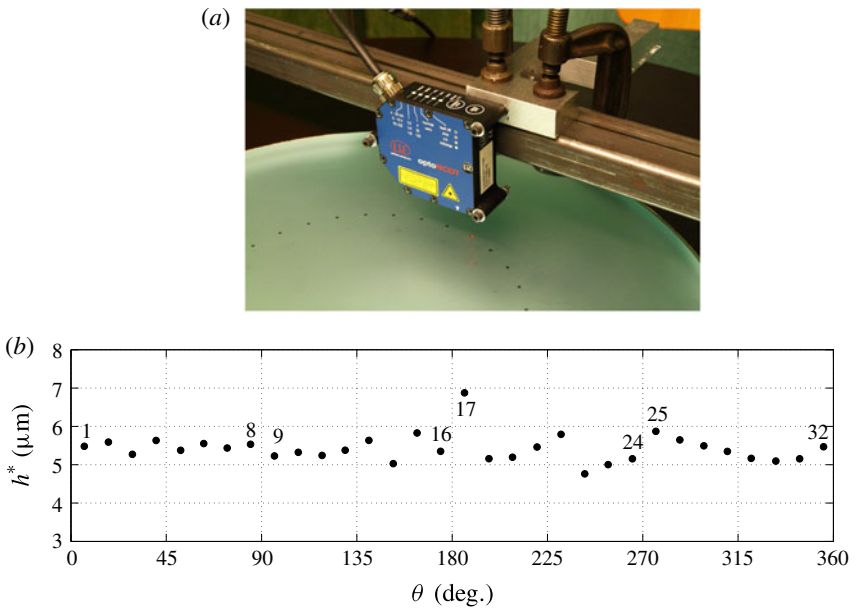


FIGURE 2. (Colour online) (*a*) Roughness-height measurement using a laser distance meter. (*b*) Measured heights, $h^*$, of roughnesses. The numbers in the figure indicate the numbering of the roughness elements.

which has a resolution of 0.5 μm. The set-up is shown in figure 2(*a*). Since the laser meter was fixed in the laboratory frame, the glass disk was rotated manually and the height was sampled with a sampling frequency of 625 Hz. The height of the roughness elements was evaluated as a relative difference between the height average of each roughness element and the neighbouring glass-disk level, and figure 2(*b*) shows the results. The averaged height of the 32 roughness elements, $\langle h^* \rangle$, is 5.4 μm and the non-dimensional height, $h = \langle h^* \rangle \sqrt{\Omega^*/\nu^*}$, is 0.014. After measurements were taken with 32 roughnesses, some of the elements were carefully removed using acetone. Then measurements were successively taken with 24, 16, 8 and 1 roughness elements; see figure 1(*b*). The clean-disk experiments were performed prior to the roughness experiments.

Table 1 describes the experimental conditions in this study. Velocity profile measurements (PP01R32–PP12R32) were performed with 32 roughness elements from $R = 335$ to $R = 555$ with intervals of $\Delta R = 20$ where $\Delta R$ is unit Reynolds number. To keep the Reynolds number at the location of the roughness elements constant, the rotational speed of the disk was fixed during the velocity profile measurements and the Reynolds number at the measurement positions was changed by varying the local radial location of a hot-wire probe. The other velocity measurements (IP01R32–IP01R01) were performed at constant height ($z = 1.3$) from $R = 260$ to $R = 605$ with intervals of $\Delta R = 5$. These measurements were also performed at a fixed rotational speed and the Reynolds number at the measurement position was changed by varying the local radial location of the probe. To compensate for slight variations in kinematic viscosity due to changes in room temperature and atmospheric pressure, the rotational speed was adjusted to keep the Reynolds number at the roughness elements constant. The data (IP01) for the clean disk are taken from measurements presented in Imayama *et al.* (2014).

| Case | $R$ | $R_{edge}$ | $r^*$ (mm) | $\Omega^*$ (r.p.m.) | $N_R$ | $z$ | $\delta_{95}$ | $\delta^*_{95}$ (mm) | $\delta^*_{1,95}$ (mm) | $\delta^*_{2,95}$ (mm) | $H_{95}$ |
|---|---|---|---|---|---|---|---|---|---|---|---|
| PP01R32 | 335 | 615 | 128 | 1015 | 32 | 0.4–10 | 3.65 | 1.40 | 0.466 | 0.211 | 2.20 |
| PP02R32 | 355 | 615 | 136 | 1015 | 32 | 0.4–10 | 3.66 | 1.40 | 0.457 | 0.212 | 2.16 |
| PP03R32 | 375 | 615 | 144 | 1015 | 32 | 0.4–10 | 3.64 | 1.39 | 0.467 | 0.211 | 2.21 |
| PP04R32 | 395 | 615 | 151 | 1015 | 32 | 0.4–10 | 3.63 | 1.39 | 0.464 | 0.211 | 2.20 |
| PP05R32 | 415 | 615 | 159 | 1015 | 32 | 0.4–10 | 3.65 | 1.40 | 0.468 | 0.211 | 2.22 |
| PP06R32 | 435 | 615 | 167 | 1015 | 32 | 0.4–10 | 3.63 | 1.40 | 0.471 | 0.211 | 2.24 |
| PP07R32 | 455 | 615 | 174 | 1015 | 32 | 0.4–10 | 3.62 | 1.39 | 0.465 | 0.213 | 2.18 |
| PP08R32 | 475 | 615 | 182 | 1015 | 32 | 0.4–16 | 3.71 | 1.42 | 0.474 | 0.224 | 2.12 |
| PP09R32 | 495 | 615 | 190 | 1015 | 32 | 0.4–16 | 4.32 | 1.66 | 0.524 | 0.263 | 1.99 |
| PP10R32 | 515 | 615 | 197 | 1015 | 32 | 0.4–20 | 8.80 | 3.37 | 0.740 | 0.471 | 1.57 |
| PP11R32 | 535 | 615 | 205 | 1015 | 32 | 0.4–20 | 12.1 | 4.62 | 0.893 | 0.620 | 1.44 |
| PP12R32 | 555 | 615 | 213 | 1015 | 32 | 0.4–20 | 14.2 | 5.45 | 1.004 | 0.708 | 1.42 |
| IP01R32 | 260–605 | 615 | 100–232 | 1013 | 32 | 1.3 | — | — | — | — | — |
| IP01R24 | 260–605 | 615 | 100–232 | 1005 | 24 | 1.3 | — | — | — | — | — |
| IP01R16 | 260–605 | 615 | 100–232 | 1005 | 16 | 1.3 | — | — | — | — | — |
| IP01R08 | 260–605 | 614 | 100–232 | 1005 | 8 | 1.3 | — | — | — | — | — |
| IP01R01 | 260–605 | 614 | 100–232 | 1013 | 1 | 1.3 | — | — | — | — | — |
| IP01 | 360–605 | 618 | 137–231 | 1000 | — | 1.3 | — | — | — | — | — |

TABLE 1. Experimental conditions. Here, $r^*$ is the local radius of the hot-wire probe, $\Omega^*$ the rotational speed, $z$ the normalized wall-normal position, $N_R$ the number of roughnesses, $\delta_{95}$ the normalized boundary-layer thickness ($\delta_{95} = \delta^*_{95}(\Omega^*/\nu^*)^{1/2}$), where $\delta^*_{95}$ is defined as the wall-normal height where the azimuthal velocity is 5 % of the disk velocity, $\delta^*_{1,95}$ the displacement thickness, $\delta^*_{2,95}$ the momentum thickness and $H_{95} = \delta^*_{1,95}/\delta^*_{2,95}$ the shape factor.

The definitions of the boundary-layer parameters, such as non-dimensional boundary-layer thickness, $\delta_{95}$, dimensional boundary-layer thickness, $\delta^*_{95}$, displacement thickness, $\delta^*_{1,95}$, momentum thickness, $\delta^*_{2,95}$, and shape factor, $H_{95}$, are the same as in Imayama *et al.* (2014). The values of these boundary-layer parameters are discussed in the next section, where they are compared with the values from the theoretical similarity profiles.

## 3. Results

This section describes the experimental results in detail, where the different roughness cases as well as the clean-disk case are compared. In addition, various aspects of the results are compared with linear stability theory. The purpose is to be able to characterize and distinguish between the convective and absolute routes to transition. Section 3.1 describes the disturbance spectra at a Reynolds number just downstream of the roughness elements for all cases including the clean-disk case. The development of the mean velocity profile for the 32-roughness case is shown in § 3.2 and compared with previous clean-disk measurements. In § 3.3 the velocity-disturbance fields, from the initiation of the disturbances to turbulent breakdown, are compared between the different roughness cases. For the 32-roughness case each individual vortex is traced and their growth rates and inclinations are compared with theory. Finally, § 3.4 describes the spectral development of the disturbances, in the linear, nonlinear and transitional regions.

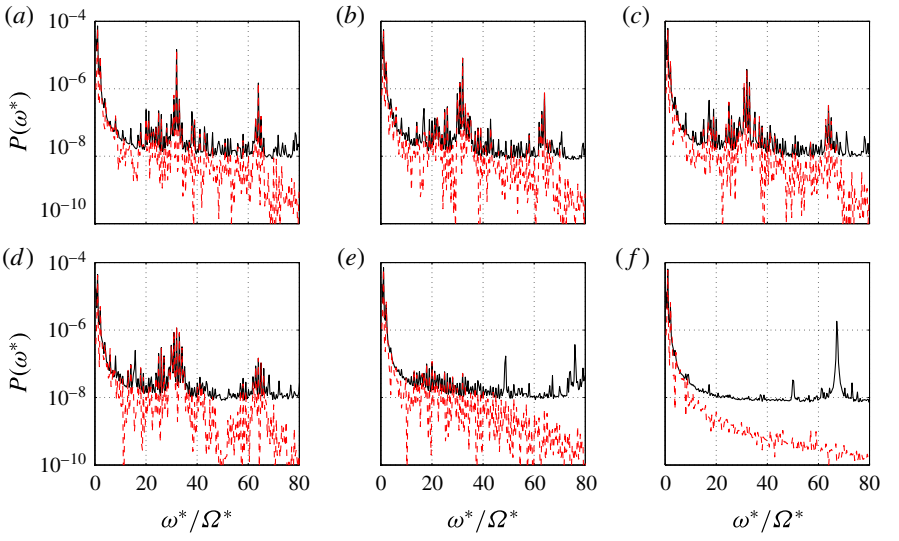


FIGURE 3. (Colour online) Spectra of single-realization (solid line) and ensemble-averaged (dashed line) time series at $R = 290$ and $z = 1.3$, showing the initial excitation by roughnesses: (*a*) 32 roughnesses [1–32], (*b*) 24 roughnesses [1–8, 17–32], (*c*) 16 roughnesses [1–8, 25–32], (*d*) 8 roughnesses [1–8], (*e*) 1 roughness [8], (*f*) 0 roughnesses (clean-disk condition).

### 3.1. *Spectra with and without surface roughness*

Figure 3 shows the spectra of the initial disturbances excited by each roughness configuration measured at $R = 290$ and $z = 1.3$. The solid (black) lines show spectra of the instantaneous (or single-realization) velocity time series from a hot-wire probe, which contain both stationary and unsteady components, and the dashed (red) lines show spectra of the ensemble-averaged velocity time series with the unsteady and travelling components averaged away. Note that the instantaneous velocity time series are the time series of a hot-wire probe in the laboratory frame at a certain radius and wall-normal height, and since the disk is moving relative to the hot-wire probe, the instantaneous velocity time series contain components that are stationary with respect to the disk and unsteady (including travelling-wave) components. The long instantaneous time series were divided into segments of 2048 samples, the spectrum for each sample length was calculated and then finally the (ensemble) average of these spectra is presented (solid line) in each subplot of figure 3. The ensemble-averaged time series were calculated by ensemble-averaging individual instantaneous time series for single revolutions of the disk, and then the dashed lines in figure 3 were calculated by taking the spectra of these ensemble-averaged time series. The ensemble averaging of time series for individual revolutions of the disk, if done over a sufficient number of time series, averages away the unsteady components that are not repeatable from one revolution to the next, leaving only those components that are repeatable, i.e. those that are fixed relative to the disk, namely the stationary components.

The peak at around $\omega^*/\Omega^* = 1$ is due to the small rotational imbalance of the disk, where $\omega^*$ is the disturbance frequency in the laboratory frame. Figure 3(*a*) shows a clear peak in both spectra at $\omega^*/\Omega^* = 32$ attributed to the 32 roughnesses, which produce disturbances that are stationary in the rotating-disk frame and, therefore,

give rise to oscillations 32 times per revolution of the disk in the laboratory frame. (Note that in the rotating frame, the 32 oscillations that are fixed relative to the disk correspond to azimuthal wavenumbers of 32 and zero disturbance frequencies.) Furthermore, it is also shown that the roughnesses excite not only $\omega^*/\Omega^* = 32$ but also other stationary modes. These spiky peaks are attributed to a superposition of unstable stationary disturbances across a range of azimuthal integer wavenumbers (in the rotating frame), as explained in the appendix of Imayama *et al.* (2014). As the number of roughnesses is decreased from 24 to 8, the mode with $\omega^*/\Omega^* = 32$ is still excited but with decreasing relative amplitude compared with other frequencies. With a single roughness element, no peak at $\omega^*/\Omega^* = 32$ is observed. This is because a single roughness element excites all wavenumbers (some growing and some decaying) and not any particular mode. With a clean disk, the stationary-disturbance amplitude indicated by the dashed line is very small compared with other cases. The peaks around $\omega^*/\Omega^* = 67$ in the spectra of instantaneous time series for the clean-disk condition and other cases are due to electrical noise from the inverter. Unlike most of the clean-disk data presented in this paper, the data for $R = 290$ in figure 3(*f*) were measured after the roughness experiments were completed.

### 3.2. *Azimuthal mean velocity profiles*

The measured azimuthal mean velocity profiles with 32 roughness elements are shown in figure 4(*a*) and the deviations of the mean velocity profiles from the theoretical laminar azimuthal profile are shown in figure 4(*b*). At low Reynolds number, there is close agreement between the measured azimuthal mean velocity profiles and the theoretical profile. The experimental non-dimensional boundary-layer thickness, $\delta_{95}$, and that for the theoretical laminar profile are shown as a dashed line with squares and a solid line, respectively. At $R = 475$ the boundary-layer thickness starts to increase in the vertical (wall-normal) direction. At higher Reynolds number, the boundary layer grows rapidly and the azimuthal velocity profile deviates from the theoretical one as shown in figure 4(*b*), and at $R = 555$ the velocity profile indicates a turbulent boundary layer. Although not presented in this paper, the azimuthal mean velocity profiles have been measured for 16 and 8 roughness elements ([1–8, 25–32], [1–8]) at $R = 395$, and those measurements confirm that the profiles match the theoretical laminar profile.

Imayama *et al.* (2014) show azimuthal mean velocity profiles for the clean-disk condition at various Reynolds number in their figure 2. In comparison, it is recognized that the transition to turbulence with 32 roughness elements occurs at lower Reynolds number. In particular, the growth of the boundary-layer thickness starts at about $R = 475$, which is lower than the onset of local absolute instability, i.e. $R_{CA} = 507$. Lingwood (1995) suggested that the local absolute instability triggers the onset of nonlinearity and transition. However, in this case, the 32 roughness elements produce relatively large-amplitude stationary disturbances in the flow field, as shown in figure 3(*a*), and Type-I stationary cross-flow instabilities grow sufficiently to trigger the onset of nonlinearity at $R < R_{CA}$. This route to laminar–turbulent transition therefore looks to be via a convectively unstable process, and occurs at lower Reynolds number than for a clean disk.

Rapid growth of the boundary-layer thickness is observed at around $R = 495$–$515$. Since the mean azimuthal velocity is calculated by azimuthally averaging instantaneous velocity measurements, the rapid growth indicates that the azimuthal variations of the transition process are small, which may be expected given that this case (PP01R32–PP12R32) is controlled by an axi-symmetric array of the 32 roughness

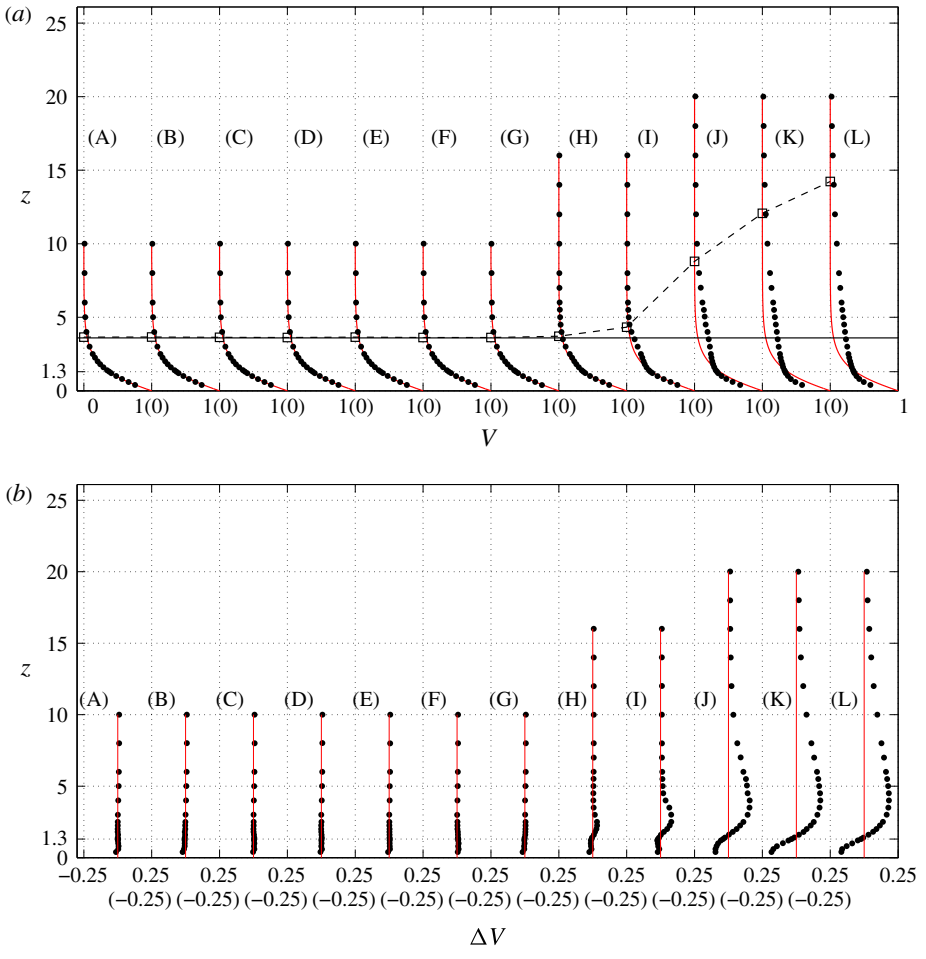


FIGURE 4. (Colour online) (*a*) Profiles of azimuthal mean velocity, $V$, (in the laboratory frame) and (*b*) deviation of azimuthal mean velocity from the theoretical laminar profile, $\Delta V$. Profiles measured for cases PP01R32–12R32 at (A) $R = 335$, (B) $R = 355$, (C) $R = 375$, (D) $R = 395$, (E) $R = 415$, (F) $R = 435$, (G) $R = 455$, (H) $R = 475$, (I) $R = 495$, (J) $R = 515$, (K) $R = 535$, (L) $R = 555$. The solid lines at each Reynolds number show the theoretical azimuthal laminar velocity profiles. The solid line at $z = 3.60$ indicates the normalized theoretical boundary-layer thickness for the laminar profile where $V$ becomes 0.05. The squares with the dashed lines show the measured boundary-layer thickness ($\delta_{95}$) given in table 1.

elements, see figure 2(*a*). As discussed later, breaking the symmetry of the surface roughnesses by removing some of them causes azimuthal variation in the transition process. However, this rapid growth in $\delta_{95}$ is also observed in the clean-disk condition, see figure 2(*a*)(I, J) in Imayama *et al.* (2014). Furthermore, Imayama *et al.* (2014) reported, for a clean disk, on the growth of both stationary and travelling instabilities in the transition regime, and showed that the stationary vortices break down independently of their individual amplitudes at around $R = 585$. So, while the boundary layers for the axi-symmetric rough disk and for the clean disk both show rapid growth, we hypothesize that this behaviour may be attributed to different

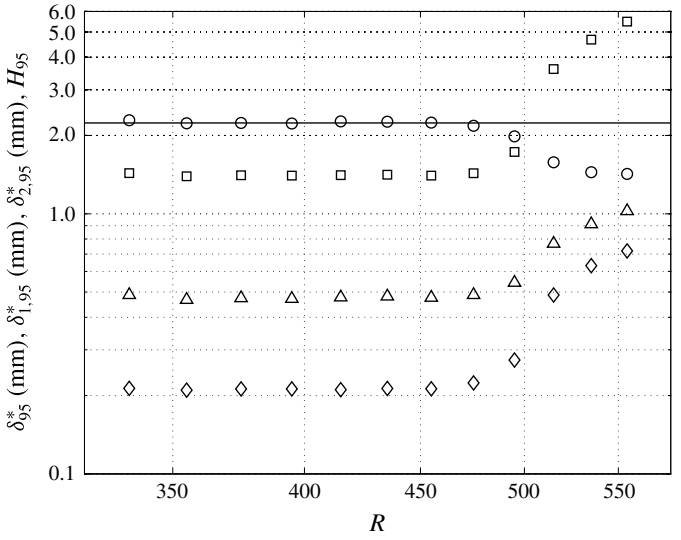


FIGURE 5. The rotating-disk boundary-layer characteristics as functions of Reynolds number on a log–log scale: □, the boundary-layer thickness, $\delta^*_{95}$; △, the displacement thickness, $\delta^*_{1,95}$; ◇, the momentum thickness, $\delta^*_{2,95}$; ○, the shape factor, $H_{95}$. The solid line shows the theoretical shape factor, $H_{95} = 2.23$, based on the boundary-layer thickness $\delta^*_{95}$. Obtained from the same data as in figure 4.

transition mechanisms. Further analysis of the stationary vortices for the rough-disk condition is discussed in § 3.3.

Figure 5 shows the boundary-layer parameters using a log–log scale; these are also shown in table 1. One of the characteristics of the similarity solution of the infinite-radius rotating-disk boundary-layer flow is that the boundary-layer thickness is constant independent of radius at fixed rotational speed and kinematic viscosity, and equivalently independent of $R$. In Imayama *et al.* (2014) velocity profile measurements were made at a fixed radial position and the Reynolds number was changed by varying the rotational speed. In the present study, a constant boundary-layer thickness was observed at low Reynolds numbers since the rotational speed was fixed and different Reynolds numbers were obtained by varying the local radial location of the hot-wire probe. The obtained shape factor, $H_{95}$, between $R = 335$ and $R = 455$ is in good agreement with the theoretical value, $H_{95} = 2.23$, shown as a solid line. Above $R = 475$, the boundary-layer thickness, displacement thickness and momentum thickness start increasing whereas the shape factor decreases. The shape factor at $R = 555$ reaches 1.42 and it is similar to the value at $R = 630$ for the clean-disk condition and in good agreement with Cham & Head's (1969) measurement results for a turbulent rotating-disk boundary-layer flow, as discussed in Imayama *et al.* (2014).

### 3.3. *Velocity-disturbance characteristics*

Measurements of the disturbance amplitude were performed for various roughness configurations and at $z = 1.3$ with intervals of $\Delta R = 5$ to investigate the laminar–turbulent transition process. To maximize the signal-to-noise ratio as in Imayama *et al.* (2014), the signals were filtered with a bandpass filter $17 < \omega^*/\Omega^* < 70$ below $R \leqslant 415$

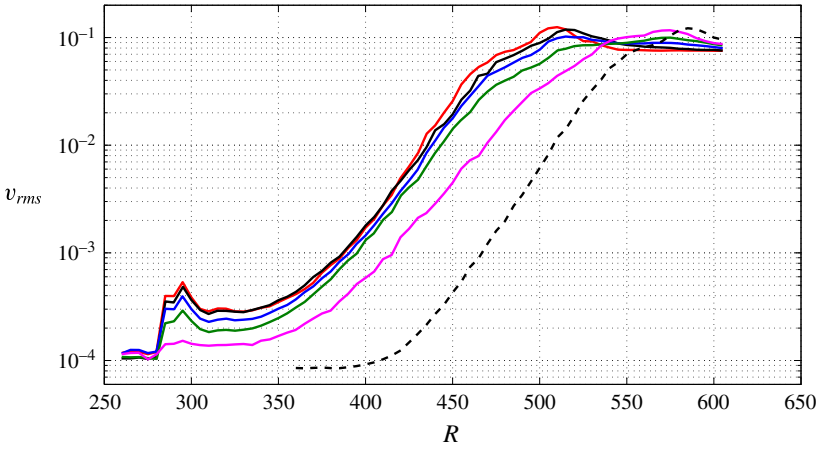


FIGURE 6. (Colour online) The $v_{rms}$ distributions measured at $z = 1.3$ with roughnesses: red solid line, 32 roughnesses [1–32]; black solid line, 24 roughnesses [1–8, 17–32]; blue solid line, 16 roughnesses [1–8, 25–32]; green solid line, 8 roughnesses [1–8]; magenta solid line, 1 roughness [8]; black dashed line, 0 roughnesses (clean-disk condition).

and with a high-pass filter $17 < \omega^*/\Omega^*$ for $420 \leqslant R \leqslant 450$ for IP01R01–IP01R32 and PP01R32–PP06R32, where $\omega^*$ is the signal frequency. The disturbance amplitude was calculated as the root-mean-square (r.m.s.) of the instantaneous velocity time series of the azimuthal fluctuation, $v^*_{rms}$, normalized by the local disk velocity, $v_{rms} = v^*_{rms}/(r^*\Omega^*)$, and is plotted in figure 6.

Figure 6 shows the roughness elements located at $R = 287$ producing stationary disturbances and $v_{rms}$ increasing from $R = 285$ to a peak at $R = 295$. The measured amplitude of the initial excitation around $R = 295$ depends on the number of roughnesses. Once the initial excitation of $v_{rms}$ has decreased beyond the roughness elements, the disturbances start increasing exponentially at around $R = 330$. Linear stability analysis (conducted in the rotating frame) shows that stationary disturbances ($\omega = 0$) with azimuthal wavenumber $\beta = 32$ become unstable at around $R = 322$. For 32 roughnesses (IP01R32) the slope of $v_{rms}$ in figure 6 changes at around $R = 455$ and a maximum in $v_{rms}$ is found at $R = 510$. As the number of roughnesses is decreased the Reynolds number of the maximum $v_{rms}$ increases, approaching the clean-disk value, and also the maximum amplitudes change.

To compare the growth of stationary disturbances generated by 32 roughness elements with local linear stability analysis, figure 7(*a*) shows a contour plot of the spectra from instantaneous velocity time series of the azimuthal fluctuation for the case IP01R32. The spectrum at each measurement Reynolds number has spiky peaks at each integer value of $\omega^*/\Omega^*$, so the maximum amplitude at each integer $\omega^*/\Omega^*$ was selected and plotted in figure 7(*a*). It is assumed that the spectra of the instantaneous time series in this figure are mainly attributable to stationary disturbances excited by roughness elements shown as spiky peaks in figure 3(*a*).

The chain line in figure 7 shows the location of the roughness elements, $R = 287$. The thick solid line denotes the neutral stability curve for stationary disturbances from local linear stability analysis using Lingwood's (1995) code. For stationary disturbances, $\omega^*/\Omega^*$ from the experiments corresponds to $\beta$ in the linear theory. The strong peak at $\omega^*/\Omega^* = 32$ is due to the 32 surface roughnesses. Growth of other

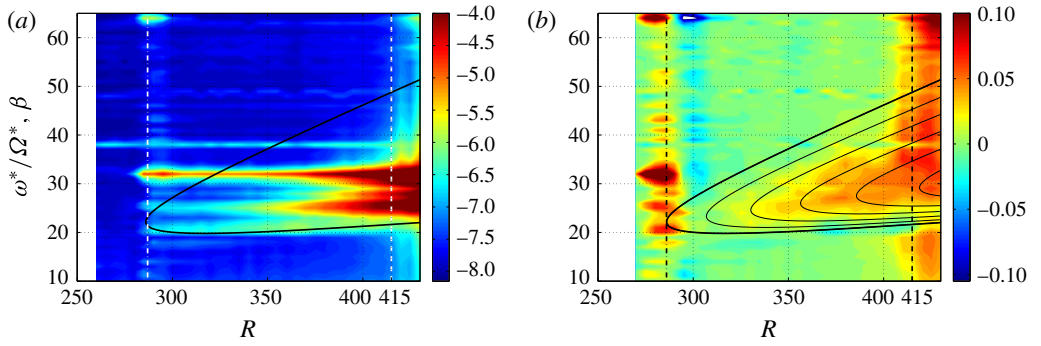


FIGURE 7. (Colour online) (*a*) Spectra $P(\omega^*)$ of instantaneous time series for case IP01R32; (*b*) radial growth rate, $-\alpha_i$, derived from (*a*). The *y*-axis shows normalized frequency (in the laboratory frame) and equivalently (provided the disturbances are fixed relative to the rotating disk) azimuthal wavenumber, $\beta$, from local stability theory (in the rotating frame). Thick black solid lines show the theoretical neutral curve inside of which the flow is convectively unstable, $-\alpha_i > 0$, i.e. there is radial spatial growth of stationary disturbances. Solid lines show radial spatial growth rates of $-\alpha_i = 0.01$, 0.02, 0.03, 0.04, 0.05 from left to right. The chain line at $R = 287$ shows the Reynolds number location of the roughnesses. The dashed line at $R = 415$ indicates the onset of nonlinearity for this case.

azimuthal modes $\omega^*/\Omega^* = 20$–30 is also observed, since the surface roughnesses at $R = 287$ excite not only $\omega^*/\Omega^* = 32$ but also other azimuthal wavenumbers as shown in figure 3(*a*). The growth of stationary disturbances is observed in the unstable region, i.e. inside the neutral curve. Figure 7(*b*) shows the radial growth rate, $-\alpha_i$, calculated as $\Delta \ln v_{rms}/\Delta R$, using $\Delta R = 20$ for each $\omega^*/\Omega^*$, from the spectra in figure 7(*a*). At around $R = 287$ the growth of disturbances is high due to the initial excitation but the modes outside the neutral curve are damped after the initial excitation. For $R = 300$–415 the observed growth rates are in excellent agreement with local linear stability theory both in terms of the distribution of unstable modes and quantitatively, as shown by comparison of the black curves of radial growth rate with the contour levels. In particular, with increasing Reynolds number the highest growth rate shifts to higher $\omega^*/\Omega^*$ as predicted by the local theory. However, at around $R = 415$, a broad range of frequencies starts growing and the experimental data do not follow local linear stability theory, indicating the onset of nonlinearity. Figure 7(*a*) also shows harmonics of the primary stationary vortices appearing around $\omega^*/\Omega^* = 64$. Using the criterion for the onset of nonlinearity given by Imayama *et al.* (2013), the onset of nonlinearity for the 32-roughness case is at $R = 415$, which is significantly lower than $R_{CA}$, and is here caused by the convective growth of stationary vortices rather than the onset of local absolute instability of travelling disturbances.

To compare disturbance profiles for stationary vortices with eigenfunctions from local stability theory, $v_{rms,st}$ profiles at $R = 335$, 355, 375 and 395 (PP01R32–PP04R32), i.e. in the linear flow region as shown by figure 7, are plotted in figure 8, where the azimuthal disturbance amplitude is obtained from the spectra of the ensemble-averaged velocity time series in the frequency range $31.5 < \omega^*/\Omega^* < 32.5$. The profiles are normalized by the maximum (peak) value. The eigenfunction of the local stationary convective instability ($R = 365$, $\omega = 0 + 0.0022\mathrm{i}$, $\alpha = 0.4388 + 0\mathrm{i}$ and $\beta = 32$) is also plotted as a dashed line. This eigenfunction was calculated using a local linear

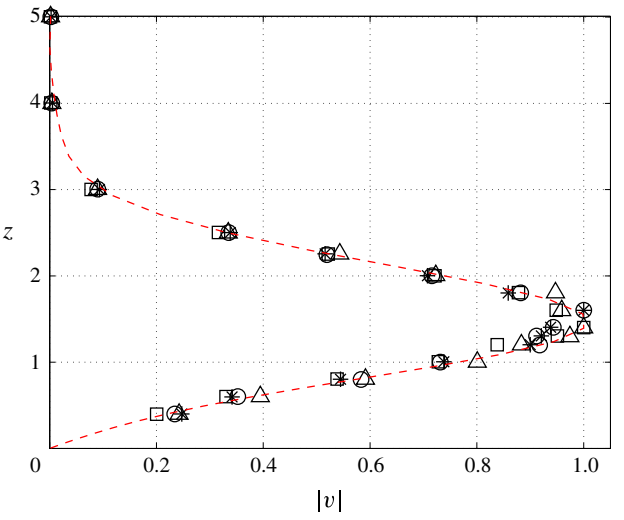


FIGURE 8. (Colour online) Profiles of azimuthal disturbance amplitude in the frequency range $31.5 < \omega^*/\Omega^* < 32.5$ measured for cases PP01R32–04R32 at $R = 335$ (□), $R = 355$ (△), $R = 375$ (○) and $R = 395$ (∗), i.e. in the linear region. The dashed line is the eigenfunction of the local stationary convective instability ($R = 365$, $\omega = 0 + 0.0022\mathrm{i}$, $\alpha = 0.4388 + 0\mathrm{i}$ and $\beta = 32$). The amplitudes are normalized by the maximum disturbance amplitude.

temporal stability code using Chebyshev polynomial discretization, and was checked against a shooting-method code, which was previously developed by Lingwood (1995). The results obtained with the two different methods were found to agree. As can be seen from figure 8, the stationary-disturbance profiles excited by 32 roughness elements are in good agreement with the eigenfunction for Type-I cross-flow stationary vortices predicted by local linear stability theory.

Figure 9 shows contour plots of the stationary-disturbance amplitude derived from ensemble-averaged velocity time series (approximately 1000 revolutions/ensemble). The black dots indicate the roughness locations at $R = 287$. With 32 roughnesses (IP01R32), breakdown of the stationary vortices is indicated by the amplitude reduction located at around $R = 520$ with no discernible azimuthal variation, which is to be expected given that the amplitudes of the stationary vortices are controlled by the axi-symmetric array of artificial surface roughnesses. For the 32-roughness case the number of stationary vortices is constant (32) from the initial excitation to breakdown. This observation contrasts with earlier experimental observations (e.g. Wilkinson & Malik 1985, Imayama *et al.* 2014), which show an increasing number of stationary vortices (usually ranging from about 22 to 32 in the linearly unstable region) as the Reynolds number increases. This is because in the present experiments the 32 mode was preferentially excited (as shown in figure 3) and, despite there being other modes with higher growth rates, the 32 mode maintains the highest amplitude up to breakdown.

Some experimental studies of the rotating-disk boundary-layer flow have captured a low-wavenumber oscillation in the breakdown region, e.g. Kobayashi, Kohama & Takamadate (1980), Corke & Knasiak (1998), Imayama *et al.* (2014). However, figure 9(*a*) does not show this kind of feature in the breakdown region. A discussion

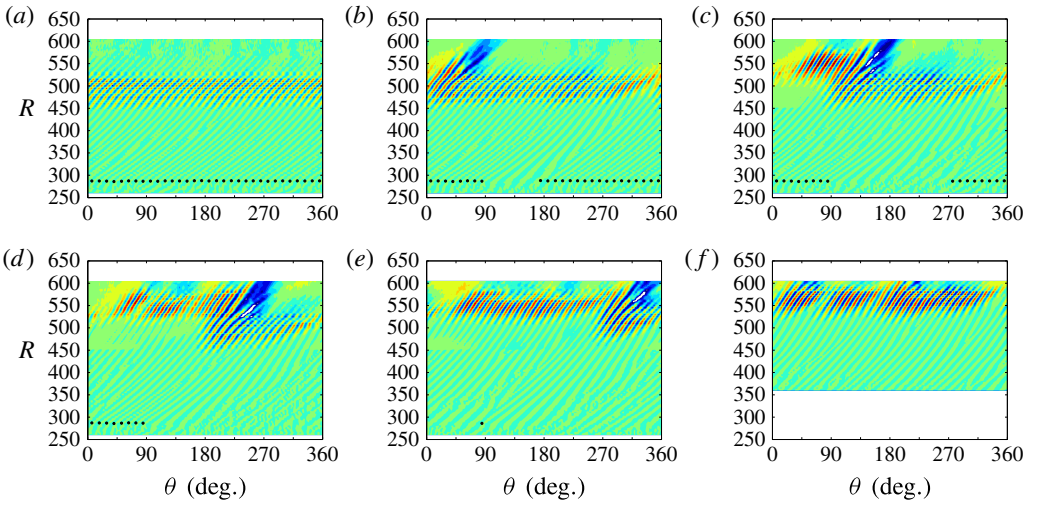


FIGURE 9. (Colour online) Stationary-vortex distributions measured at $z = 1.3$ at radial steps of $\Delta R = 5$: (*a*) 32 roughnesses [1–32], (*b*) 24 roughnesses [1–8, 17–32], (*c*) 16 roughnesses [1–8, 25–32], (*d*) 8 roughnesses [1–8]; (*e*) 1 roughness [8], (*f*) 0 roughnesses (clean-disk condition). The filled contours from blue to red (colour online) indicate −0.12, −0.1, −0.08, −0.06, −0.04, −0.02, 0, 0.02, 0.04, 0.06, 0.08, 0.1, 0.12 of the ensemble-averaged fluctuation velocity normalized by the local wall speed. The dots indicate locations of roughnesses (the size is not to scale).

of this large-scale stationary structure is given in § 3.4 together with spectra of azimuthal velocity time series.

Removing some of the surface roughness elements results, as shown in figure 9(*b–e*), in the breakdown locations of the stationary vortices moving downstream and approaching the clean-disk condition in figure 9(*f*). The convective behaviour of the stationary vortices generated by the roughness elements is clearly shown by figure 9. The angular variations in the azimuthal wavenumber in regions excited by the artificial roughnesses compared with regions not artificially excited are also evident in figure 9(*b–d*) at around $R = 287$. The naturally most unstable stationary azimuthal wavenumber at the onset of convective instability is around $\beta = 22$, which is close to the wavenumber observed in figure 9(*b–d*) at low $R$ in the gap between roughnesses.

In the breakdown and turbulent regions in figure 9(*b–e*) a large-scale stationary structure is captured. The azimuthal location of the structure seems to be dependent on the positioning of the roughness elements, and particularly linked to the leading roughness element. Figure 9(*b–e*) shows that the azimuthal position of the large structure shifts to the right (positive $\theta$ direction) as the leading roughness position moves in the same direction (namely, linked to roughness numbers 17 in (*b*), 23 in (*c*), 1 in (*d*) and 8 in (*e*)).

Figure 10(*a*) shows the same data as in figure 9(*a*) but in the circular geometry, namely stationary disturbances from ensemble-averaged velocity time series of the azimuthal fluctuation at $z = 1.3$ with 32 roughness elements (IP01R32). Black dots indicate the locations of the roughness elements. The amplitude of the stationary disturbances reaches a maximum at around $R = 500$ and then decreases as the stationary vortices break down. Figure 10(*a*) is comparable with figure 12(*a*) in

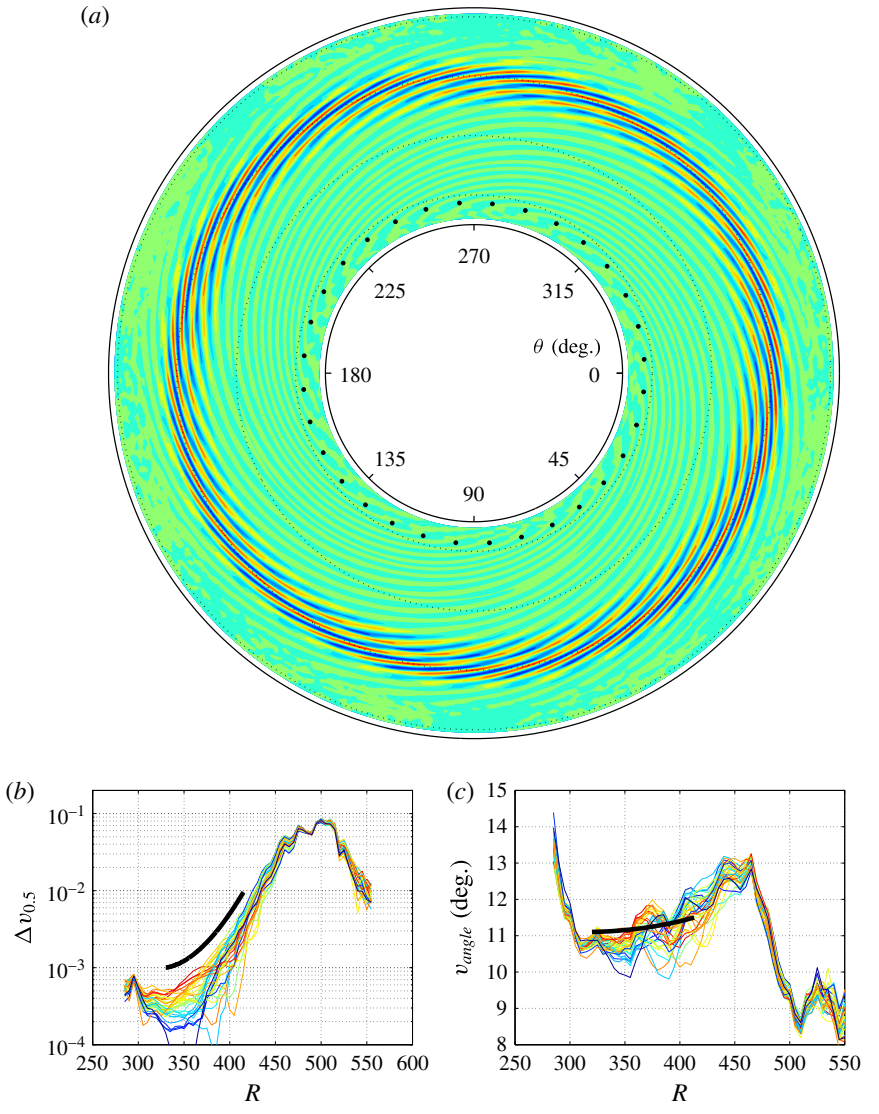


FIGURE 10. (Colour online) Stationary-vortex characteristics with 32 roughnesses [1–32] measured at $z = 1.3$ with a radial step of $\Delta R = 5$. (*a*) Stationary-vortex distributions. The filled contours from blue to red indicate the ensemble-averaged fluctuation velocity normalized by the local wall speed at $-0.12$, $-0.1$, $-0.08$, $-0.06$, $-0.04$, $-0.02$, 0, 0.02, 0.04, 0.06, 0.08, 0.1, 0.12. Dotted lines in (*a*) indicate $R = 300$, 400, 500, 600, respectively, moving outward. The edge of the disk, i.e. $R = 615$, is shown as the outer solid circle in (*a*). The positions of the roughness elements are shown as the black dots (the scale is not actual scale). (*b*) Each stationary-vortex amplitude, $\Delta v_{0.5}$, where the colour indicates the amplitude of $\Delta v_{0.5}$ at $R = 350$. The solid line shows the disturbance amplitude calculated from the radial growth rate of linear stability analysis for $\beta = 32$; note that the vertical position is arbitrary. (*c*) The angle distributions of each stationary vortex, where the colour indicates the reference amplitude shown in (*b*). The solid line shows the angle predicted by local linear stability analysis for $\beta = 32$.

Imayama *et al.* (2014), which also shows stationary disturbances but for the clean disk. In both cases, very little azimuthal variation is observed, but here that is due to the controlling effect of the 32 roughness elements located in an equi-angular arrangement. While also largely independent of angular position, this is in contrast to the mechanism depicted in figure 12(*a*) in Imayama *et al.* (2014) for the clean disk where the stationary vortices break down independently of their amplitude but at a fixed $R$. Figure 10(*b*) shows peak-to-peak amplitudes of each stationary vortex, $\Delta v_{0.5}$, measured at $z = 1.3$; the same quantity is presented in figure 13(*a*) in Imayama *et al.* (2014) for the clean-disk condition. These results are compared with the disturbance amplitude calculated from the radial growth rate of linear stability analysis for $\beta = 32$ shown as the thick solid line (note that the vertical position is arbitrary). At around $R = 500$, the nonlinear-saturation region of the stationary vortices shows qualitatively and quantitatively similar behaviour for all stationary vortices, as is expected given the axi-symmetric roughness array. Comparing figure 10(*b*) with figure 13 in Imayama *et al.* (2014) for the clean disk shows that the amplitude behaviour in the nonlinear-saturation region here has slightly greater amplitude variation (for clearer figures, see figures 10 and 11 in paper 3 in Imayama (2012)). The angle distributions are also presented in figure 10(*c*) and, for the linearly unstable region, they are in good agreement with the angle predicted by local linear stability analysis shown as a solid line.

### 3.4. *Comparisons of velocity-disturbance spectra*

In the previous section, the properties of artificially excited stationary disturbances were described and found to be in good agreement with results of local linear stability theory. Here, in this section, comparisons of the spectra for the different roughness configurations are given to explain the potential competition between laminar–turbulent transition routes for the rotating-disk boundary-layer flow, in particular comparing the convectively and absolutely unstable transition routes.

The cases of 32, 8 and 0 roughnesses are chosen for comparison. Figure 11(*a*) shows the development of $v_{rms}$ at $z = 1.3$ for these three conditions. Spectral comparisons are made at three selected $v_{rms}$ amplitudes shown as dashed lines. For example, in figure 11(*a*), (A, B, C), which are for $R = 360$, 370, 450, respectively, are selected to compare the spectra from the three different roughness cases. (D, E, F) and (G, H, I) are selected in a similar way. Figure 11(*b*) shows the spectra obtained both from ensemble-averaged time signals and from the original time signals. In all cases, the peak at around $\omega^*/\Omega^* \approx 1$ is due to the small rotational imbalance of the disk (note different vertical scales for the three rows). In figure 11(*b*)(A, B, C), the spiky peaked region centred around $\omega^*/\Omega^* \approx 30$ is observed for both single-realization and ensemble-averaged time series. This indicates that the peaks are due to stationary disturbances rather than travelling ones, since travelling disturbances are averaged away in the ensemble-averaging process. For all three cases, (A, B, C), the peaks in the high-resolution spectra are spiky because the stationary-vortex field is composed of a superposition of multiple unstable integer azimuthal wavenumbers excited by surface roughnesses, which a hot-wire probe records as a frequency-modulated time series; see Imayama *et al.*'s (2014) appendix. At this amplitude the qualitative characteristics of these spectra are similar across the roughness configurations.

The spectra for cases (D, E, F) are at higher amplitude than (A, B, C). The Reynolds numbers corresponding to (D, E, F) are $R = 435$, 450, 510, respectively. At this amplitude, harmonics of the primary spectral contribution from the stationary

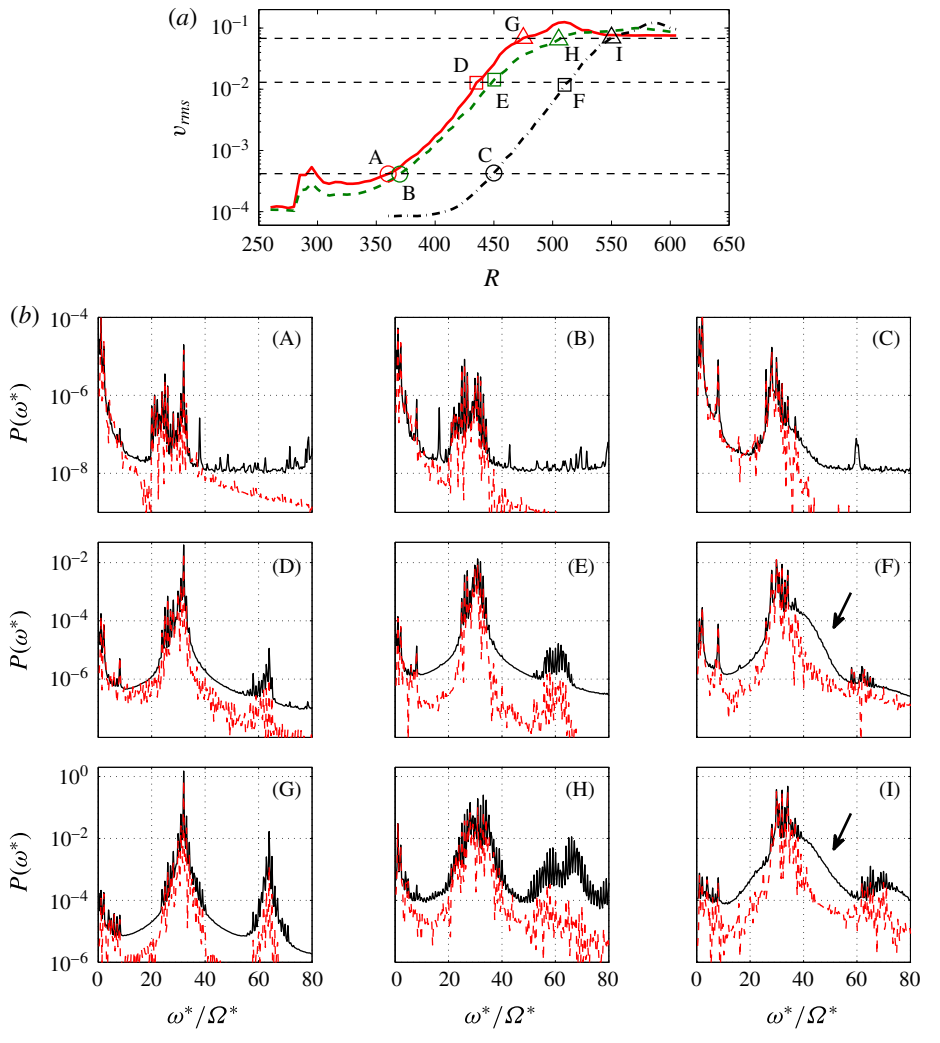


FIGURE 11. (Colour online) The disturbance growth and spectra corresponding to the marked Reynolds numbers and roughness cases. (*a*) $v_{rms}$ measured at $z = 1.3$: red solid line, 32 roughnesses [1–32]; green solid line, 8 roughnesses [1–8]; black solid line, 0 roughnesses (clean-disk condition). The conditions labelled A–I are selected to allow comparison of the spectral characteristics of each roughness configuration. (*b*) Spectra of single-realization (solid line) and ensemble-averaged (dashed line) time series for different roughness configurations: (A, D, G) 32 roughnesses [1–32]; (B, E, H) 8 roughnesses [1–8]; (C, F, I) 0 roughnesses (clean-disk condition). Labels (A–I) correspond to those in (*a*).

vortices are observed at around $\omega^*/\Omega^* = 60$. This indicates the appearance of nonlinearity. In cases (D, E), the onset of nonlinearity occurs at lower $R$ than the onset of local absolute instability, $R_{CA} = 507.3$, which allows us to attribute the onset of nonlinearity to the growth of Type-I cross-flow instability excited by the surface roughnesses. However, in (F), for the clean disk, a new feature is captured in the spectrum at $R = 510$ indicated by the arrow, i.e. a smooth elevated region in the spectrum of the instantaneous time series. This smooth peak was first found in

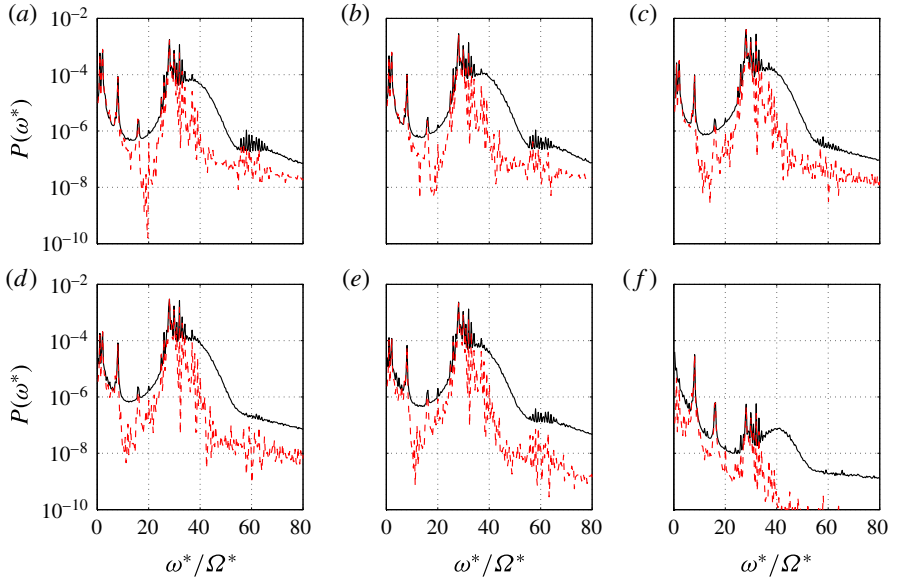


FIGURE 12. (Colour online) Spectra of single-realization (solid line) and ensemble-averaged (dashed line) time series for the clean-disk condition at $R = 510$ and (*a*) $z = 0.6$, (*b*) $z = 0.8$, (*c*) $z = 1.3$, (*d*) $z = 1.6$, (*e*) $z = 2.0$, (*f*) $z = 4.0$.

Imayama *et al.* (2014), where it was shown that it is due to a travelling mode rather than a stationary one since it is not captured in the spectra of ensemble-averaged time series. At higher amplitudes, at $R = 475$, 505, 550, the development of $v_{rms}$ shows a change of slope in figure 11(*a*), and for cases (G, H, I) the corresponding spectra are shown. The growth of stationary disturbances with $R$ is evidenced by the spiky spectra in (G, H), whereas for the clean disk the growth of both stationary and travelling disturbances is shown in figure 11(*b*)(I). For case (H), the spectra are very spiky, in particular for the instantaneous time series. This may be caused by the strong asymmetry in roughness (figure 1*b* (D)), resulting in asymmetry of the stationary-vortex distribution. Similar results were captured in Siddiqui *et al.* (2013). Spectra in their figure 5 showed the onset of nonlinearity before $R_{CA}$ and also spiky peaks at various $\omega^*/\Omega^*$ similar to case (H).

To investigate the characteristics of the smooth peak captured in figure 11(*b*)(F) further, figure 12 shows spectra of single-realization and ensemble-averaged time series measured at $R = 510$ at various wall-normal heights. In addition to the spiky peaks, smooth peaks centred on $\omega^*/\Omega^* \approx 40$ are also observed only in the spectra of single-realization time series. These smooth peaks are more obvious at higher wall-normal positions and are due to travelling disturbances (as they are not shown in spectra of ensemble-averaged time series). Although the observed frequency of about $\omega^*/\Omega^* \approx 40$ does not fully agree with theoretical prediction of the local absolute instability ($\omega^*/\Omega^* = 50.3$ at $R_{CA}$) by Lingwood (1997), Imayama *et al.* (2014) discussed that 'this perhaps corresponds to the global mode realized in the physical flow, which has a more complex base flow than accounted for in theoretical analyses due, for example, to unavoidable convectively unstable stationary vortices'. The harmonics of these primary peaks are also shown in figure 12, indicating the appearance of nonlinearity, which is highly repeatable for the clean rotating-disk

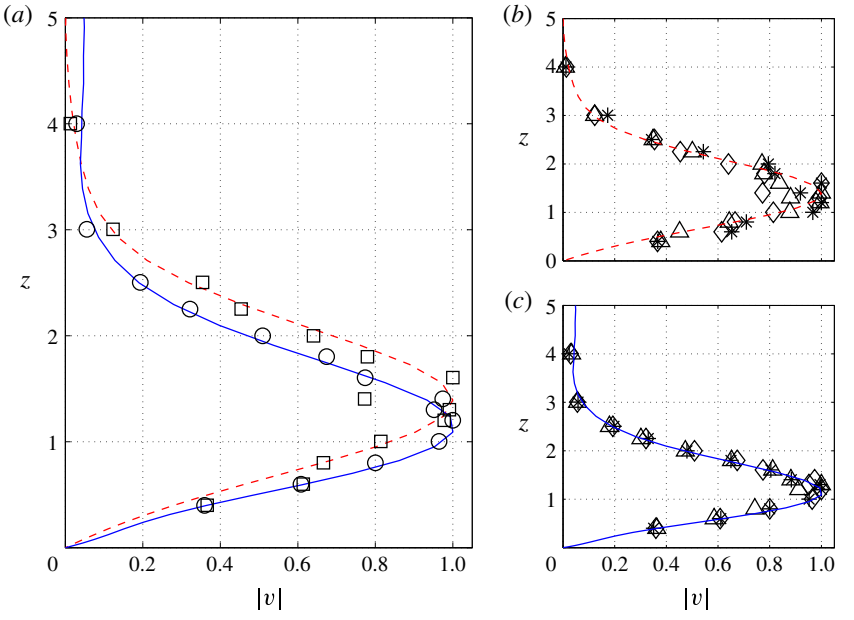


FIGURE 13. (Colour online) Profiles of azimuthal disturbance amplitude from the clean-disk condition. The stationary-disturbance amplitude is obtained by bandpass filtering in the frequency range $31.5 < \omega^*/\Omega^* < 32.5$, whereas the travelling disturbance amplitude is obtained from the frequency range $40 < \omega^*/\Omega^* < 50$. The solid line is the theoretical eigenfunction of the local absolute instability at $R_{CA}$ obtained with parameters from Lingwood (1997). The dashed line is the eigenfunction of the local convective instability for stationary disturbances ($R = 507.3$, $\omega = 0.00447\mathrm{i}$, $\alpha = 0.268$ and $\beta = 31$). The amplitudes are normalized by the maximum disturbance amplitude. (*a*) □, stationary disturbance; ○, travelling disturbance profiles at $R = 510$. (*b*) Stationary-disturbance profiles at $R = 490$ (△), $R = 510$ (◇), $R = 530$ (∗). (*c*) Travelling disturbance profiles. The symbols are the same as in (*b*).

flow. As shown in figures 5 and 6 of Imayama *et al.* (2014), for a clean disk and Reynolds numbers above $R \approx 510$ the nonlinear effects for both stationary and travelling instabilities become dominant and the flow undergoes transition to turbulence.

Imayama *et al.* (2014) showed wall-normal profiles of the unsteady disturbance at several Reynolds numbers in their figure 7. Since the unsteady components contain not only travelling disturbances but also unsteadiness of stationary ones, here, in order to extract purely travelling disturbances from the single-realization time series, bandpass filtering over the range of $40 \leqslant \omega^*/\Omega^* \leqslant 50$ was applied. Figure 12 shows that over this range of frequencies the signal is mainly composed of travelling disturbances.

Figure 13(*a*) shows profiles of stationary and travelling disturbances at $R = 510$ from our experiments and eigenfunctions from linear stability theory of the stationary convective instability mode and the critical absolute instability mode. The profiles for the stationary disturbance were filtered in the same way as in figure 8. The profiles in figure 13 are normalized by the maximum amplitude of each profile. The eigenfunction for the stationary mode is calculated with the following parameters: with $R$ and $\beta$ fixed at 507.3 and 31, respectively, with the real part of $\omega_c$, which is the angular frequency of the disturbance in the rotating frame, set to zero, and

solving temporally for real $\alpha$ (radial wavenumber) and imaginary $\omega_c$, giving $\alpha = 0.268$ and $\omega_c = 0.00447\mathrm{i}$. The parameters for the critical absolute instability are given by Lingwood's (1997) table 3. The experimental profile for the stationary disturbances corresponds to the eigenfunction of the stationary mode very closely. Furthermore, the experimental profile for the travelling disturbances is in excellent agreement with the distinct eigenfunction of the critical absolute instability mode. The excellent correspondence between experimental and theoretical results shown in figure 13 indicates that the observed travelling disturbances shown by the smooth peaks in figure 12 are attributable to the absolute instability. This is the first such experimental observation of a global mode directly attributable to the absolute instability of the 'unexcited' rotating-disk boundary-layer flow. Figure 13(*b*,*c*) shows similar profiles to figure 13(*a*) but at $R = 490$, 510, 530 together with their respective eigenfunctions. The profiles are normalized by each identified maximum amplitude as in figure 13(*a*). At each Reynolds number the experimental data adhere nicely to the theoretical eigenfunctions. Although the local absolute instability only exists above $R_{CA}$, as observed in the numerical study between two rotating disks (i.e. in an open rotating cavity) by Viaud, Serre & Chomaz (2008), the global mode is expected to connect smoothly to the upstream convectively unstable region, giving a nonlinear front straddling $R_{CA}$. Therefore, as expected, the profile of the travelling disturbance at $R = 490$ indicates the upstream matching between travelling convectively and absolutely unstable regions.

Figures 12 and 13(*a*) here, and figure 6 in Imayama *et al.* (2014), show that, for the clean-disk condition, travelling disturbances due to the absolute instability emerge at $R \approx 510$ and the latter paper (Imayama *et al.* 2014) shows that the total disturbance field saturates nonlinearly at a well-defined Reynolds number independent of the amplitude of stationary disturbances. This evidence of the influence of a travelling global mode supports Lingwood's (1995) hypothesis that (for a clean disk) the local absolute instability above $R_{CA}$ triggers the onset of nonlinearity and transition to turbulent flow. There is some debate about the route to nonlinearity, i.e. whether that could be via a linear global instability (Healey 2010; Appelquist *et al.* 2015) or whether it is via a nonlinear global mode (Pier 2003). In either case the global mode would be located by $R_{CA}$. For example, Huerre & Monkewitz (1990) suggested that the global behaviour in spatially developing flows acts as 'self-excited, low-amplitude wavemaker in the region of local absolute instability'. Pier & Huerre (2001) proposed that 'nonlinear global instability takes place as soon as local absolute instability arises at some point in the flow' and Pier, Huerre & Chomaz (2001) also suggested that 'the front acts as a wavemaker which sends out nonlinear travelling waves in the downstream direction', the so-called primary nonlinear steep-fronted global mode (Pier *et al.* 1998; Pier 2003). The present experimental results, the emergence of a travelling global mode and the onset of nonlinearity, align with these theories on front dynamics at the boundary between local convective and absolute instability.

For comparisons of the later stage of the transition process for the three different roughness configurations, figure 14(*a*) shows the $v_{rms}$ distributions for the cases of 32, 8 and 0 roughnesses at higher Reynolds number than figure 11(*a*). At this stage of the transition process, data for the comparisons are selected to give similar points in the transition process rather than for their amplitudes.

Figure 14(*b*)(J, K, L) corresponds to $R = 495$, 545, 570, respectively. (J) presents a relatively narrow peak at $\omega^*/\Omega^* = 32$ and the harmonics indicate strong nonlinearity. The spectrum of the instantaneous time series for case (K) shows that energy is distributed across a broad frequency range because breakdown of the stationary

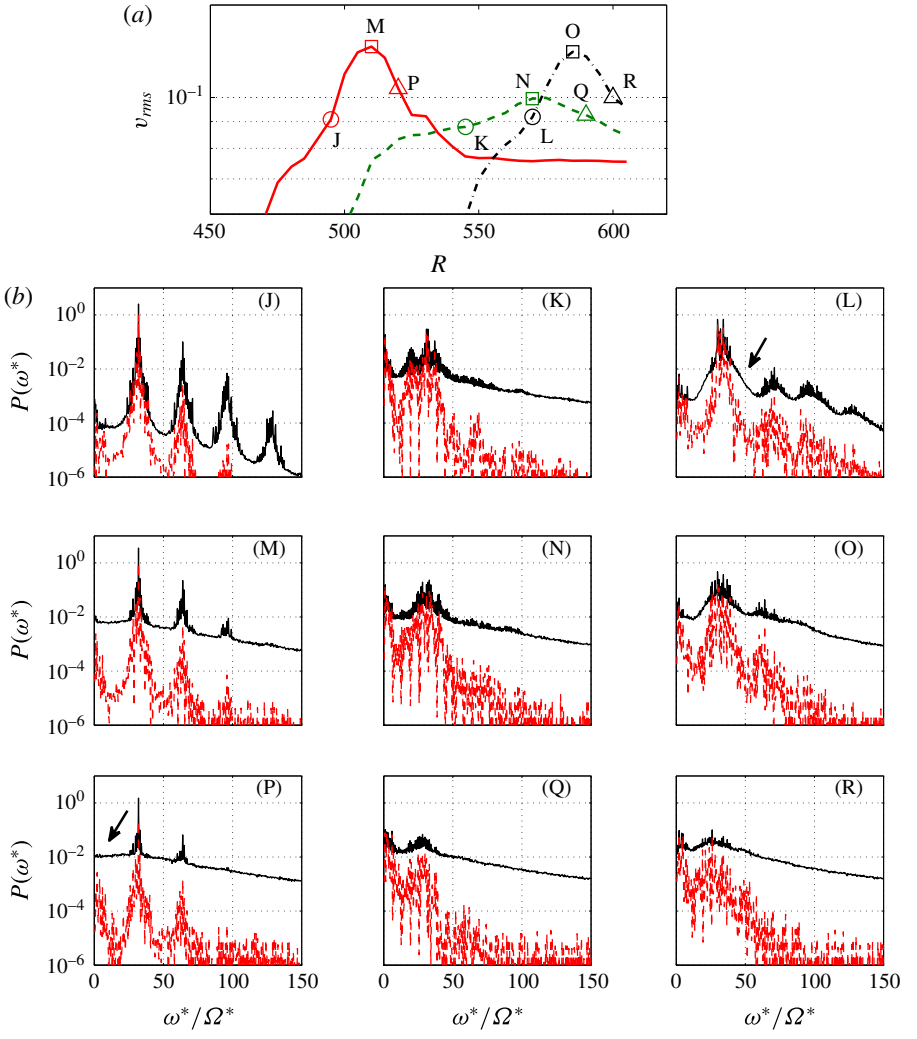


FIGURE 14. (Colour online) The disturbance growth and spectral comparisons at a later stage of the transition process. (*a*) $v_{rms}$ measured at $z = 1.3$: red solid line, 32 roughnesses [1–32]; green dashed line, 8 roughnesses [1–8]; black chained line, 0 roughnesses (clean-disk condition). $v_{rms}$ labelled by J–R are selected to compare the spectral characteristics of each roughness configuration. (*b*) Spectra of single-realization (solid line) and ensemble-averaged (dashed line) time series for different roughness configurations: (J, M, P) 32 roughnesses [1–32]; (K, N, Q) 8 roughnesses [1–8]; (L, O, R) 0 roughnesses (clean-disk condition). Labels (J–R) correspond to those in (*a*).

vortices excited by eight roughness elements has already occurred, as shown in figure 9(*d*). However, figure 9(*d*) also shows that the region that is not influenced by the roughnesses has yet to break down at this Reynolds number ($R = 545$). This azimuthal variation in amplitude of stationary disturbances could cause these spiky peaks across the broad frequency range. The spectrum of the instantaneous time series in figure 14(*b*)(L) for the clean disk perhaps also captures the growth of a smooth part of the spectrum attributed to the global mode, as indicated by the arrow.

The cases (M, N, O) correspond to $R = 510$, 570, 585, respectively, where the maximum $v_{rms}$ are observed for the three roughness cases. Spectra of instantaneous time series in these figures capture the growth of energy across a broad frequency range, indicating breakdown to turbulence. Finally, (P, Q, R) show the final stage of the laminar–turbulent transition, corresponding to $R = 520$, 590, 600, respectively. It is recognized that the maximum value (excluding peaks at 32 etc.) of $P(\omega^*)$ from the ensemble-averaged time series in (P) is lower than for the two other cases (Q, R), as indicated by the arrow in (P). These low-frequency contributions correspond to the large-scale stationary structures that can appear at breakdown and in the turbulent region of the rotating-disk flow, as discussed in earlier sections of this paper and other papers (Kobayashi *et al.* 1980; Corke & Knasiak 1998; Imayama *et al.* 2014). The main difference between (P) and (Q, R) is the azimuthal variation of the stationary-disturbance amplitude, as shown in figure 9, which, therefore, appears to be important for the growth of these large-scale stationary structures. This finding is not inconsistent with Corke & Knasiak's (1998) suggestion that resonance between stationary and travelling modes is the trigger.

## 4. Conclusions

In the present paper, an extensive experimental study has been performed of rotating-disk boundary-layer flow with surface roughnesses. The motivation for the rough-disk study was to excite Type-I stationary disturbances and to investigate the transition to turbulence via a convectively unstable route. Several roughness cases were studied, starting with 32 equally spaced roughnesses with an average height of 5.4 μm at $R = 287$. Then the number of roughnesses was reduced by removing some of the 32 roughnesses. In the linear regime, the excited stationary disturbances are in excellent agreement with local linear stability theory in terms of growth rate and eigenfunctions. With artificial roughness elements on the disk surface, the transition to turbulence occurs earlier than for a clean disk and proceeds via a convective route before the flow can become locally absolutely unstable. The contour map of ensemble-averaged time series in figure 9 clearly shows the convective behaviour of the stationary vortices as the number of roughness elements is reduced. The leading edge of the array of roughness elements is shown to create a wedge-like large stationary structure in both the breakdown and turbulent regions of the flow.

Spectral comparisons for different roughness configurations, in particular with and without artificial roughnesses, were performed to investigate the two competing transition mechanisms, i.e. convectively unstable transition and absolutely unstable transition. Without roughness elements, given the smoothness of the disk and the nature of our experimental findings, our results are considered to fall into the clean-disk category. The differences are clearly captured at the onset of nonlinearity. With the surface roughness elements, the onset of nonlinearity is observed at lower Reynolds number than the onset of local absolute instability. The spectra show only spiky peaks attributed to the superposition of multiple unstable stationary disturbances with integer azimuthal wavenumber, which indicates that the nonlinearity is caused by the growth of Type-I cross-flow stationary vortices. However, for the clean disk, the spectra of the instantaneous time series show the emergence of a smooth peak at around $\omega^*/\Omega^* = 40$, which was shown to be due to travelling disturbances in Imayama *et al.* (2014). The emergence of the travelling instability and corresponding onset of nonlinearity is evidence of the absolute instability and is in contrast to the rough-disk case.

To elaborate further on the travelling disturbances, the spectra of azimuthal instantaneous fluctuation velocity at $R = 510$ (at various $z$) are shown. These spectra have spiky and smooth peaks representing stationary and travelling instabilities, respectively, with the travelling instabilities showing more clearly at higher $z$. Profiles of the azimuthal fluctuation velocity of the travelling disturbances are produced by applying a bandpass filter. Profiles of the azimuthal fluctuation velocity of the stationary disturbances are also shown. These experimental profiles are compared with eigenfunctions calculated from local linear stability theory. It is found that the experimental profile of the travelling disturbances is in excellent agreement with the theoretical eigenfunction of the critical local absolute instability. The profiles of the stationary disturbances agree very well with the distinct stationary convective eigenfunction.

At the later stage of transition, it was found that the large-scale stationary structure observed in the breakdown region is significantly damped in the 32-roughness case. This observation is in contrast to other roughness configurations including the clean-disk condition (Imayama *et al.* 2014) and other experimental studies (Kobayashi *et al.* 1980; Corke & Knasiak 1998; Corke & Matlis 2006; Corke *et al.* 2007). Corke and co-workers suggested that the large stationary structure in the breakdown region is due to interactions (resonances) between stationary and travelling instabilities. Here, our experimental results show that the variation in azimuthal amplitude of the stationary disturbances is an important factor in the emergence of the large-scale structure, but this is not necessarily inconsistent with resonance being a causal factor.

The presented results show that the flow is sensitive to surface roughness, i.e. very little roughness height is required to trigger strong Type-I cross-flow stationary vortices. Less attention to treatment of surface roughness may easily cause transition to turbulence via a convectively unstable route. However, if the surface of the disk is smooth and clean enough, the flow remains linear up to high $R$, which allows for the emergence of travelling disturbances. The present results for a clean disk are briefly compared with theoretical studies of global behaviours in spatially developing flow and found to be in good qualitative agreement. They show the onset of nonlinearity at $R \approx 510$ and a clear link from the onset of local absolute instability to the nonlinear (travelling) global mode. This may explain the high repeatability in Reynolds number for the onset of transition of rotating-disk boundary layers reported by Imayama *et al.* (2013) in different facilities with smooth clean disks.

## Acknowledgements

This work is supported by the Swedish Research Council (VR) and the Linné FLOW Centre. Stimulating discussions with E. Appelquist are gratefully acknowledged. We also acknowledge A. Segalini who helped to develop the code for the linear stability analysis using a Chebyshev discretization method.

## REFERENCES

APPELQUIST, E., SCHLATTER, P., ALFREDSSON, P. H. & LINGWOOD, R. J. 2015 Global linear instability and the radial boundary of the rotating-disk flow. *J. Fluid Mech.* **765**, 612–631.

CHAM, T.-S. & HEAD, M. R. 1969 Turbulent boundary-layer flow on a rotating disk. *J. Fluid Mech.* **37**, 129–147.

CORKE, T. C. & KNASIAK, K. F. 1998 Stationary travelling cross-flow mode interactions on a rotating disk. *J. Fluid Mech.* **355**, 285–315.

CORKE, T. C. & MATLIS, E. H. 2006 Transition to turbulence in 3-D boundary layers on a rotating disk – triad resonance. In *IUTAM Symposium on 100 Years of Boundary Layer Research* (ed. G. E. A. Meier & K. R. Sreenivasan), pp. 189–199. Springer.

CORKE, T. C., MATLIS, E. H. & OTHMAN, H. 2007 Transition to turbulence in rotating-disk boundary layers – convective and absolute instabilities. *J. Engng Maths* **57**, 253–272.

DAVIES, C. & CARPENTER, P. W. 2003 Global behaviour corresponding to the absolute instability of the rotating-disc boundary layer. *J. Fluid Mech.* **486**, 287–329.

FALLER, A. J. 1991 Instability and transition of disturbed flow over a rotating disk. *J. Fluid Mech.* **230**, 245–269.

GREGORY, N., STUART, J. T. & WALKER, W. S. 1955 On the stability of three-dimensional boundary layers with application to the flow due to a rotating disk. *Phil. Trans. R. Soc. Lond.* **248**, 155–199.

HEALEY, J. J. 2010 Model for unstable global modes in the rotating-disk boundary layer. *J. Fluid Mech.* **663**, 148–159.

HUERRE, P. & MONKEWITZ, P. A. 1990 Local and global instabilities in spatially developing flows. *Annu. Rev. Fluid Mech.* **22**, 473–537.

HUSSAIN, Z., GARRETT, S. J. & STEPHEN, S. O. 2011 The instability of the boundary layer over a disk rotating in an enforced axial flow. *Phys. Fluids* **23**, 114108.

IMAYAMA, S. 2012 Experimental study of the rotating-disk boundary-layer flow. Lic. Thesis, KTH Mechanics.

IMAYAMA, S., ALFREDSSON, P. H. & LINGWOOD, R. J. 2012 A new way to describe the transition characteristics of a rotating-disk boundary-layer flow. *Phys. Fluids* **24**, 031701.

IMAYAMA, S., ALFREDSSON, P. H. & LINGWOOD, R. J. 2013 An experimental study of edge effects on rotating-disk transition. *J. Fluid Mech.* **716**, 638–657.

IMAYAMA, S., ALFREDSSON, P. H. & LINGWOOD, R. J. 2014 On the laminar-turbulent transition of the rotating-disk flow: the role of absolute instability. *J. Fluid Mech.* **745**, 132–163.

VON KÁRMÁN, T. 1921 Über laminare und turbulent Reibung. *Z. Angew. Math. Mech.* **1**, 233–252.

KOBAYASHI, R., KOHAMA, Y. & TAKAMADATE, C. 1980 Spiral vortices in boundary layer transition regime on a rotating disk. *Acta Mechanica* **35**, 71–82.

LINGWOOD, R. J. 1995 Absolute instability of the boundary layer on a rotating disk. *J. Fluid Mech.* **299**, 17–33.

LINGWOOD, R. J. 1996 An experimental study of absolute instability of the rotating-disk boundary-layer flow. *J. Fluid Mech.* **314**, 373–405.

LINGWOOD, R. J. 1997 Absolute instability of the Ekman layer and related rotating flows. *J. Fluid Mech.* **331**, 405–428.

MALIK, M. R., WILKINSON, S. P. & ORSZAG, S. A. 1981 Instability and transition in rotating disk flow. *AIAA J.* **19**, 1131–1138.

OTHMAN, H. & CORKE, T. C. 2006 Experimental investigation of absolute instability of a rotating-disk boundary layer. *J. Fluid Mech.* **565**, 63–94.

PIER, B. 2003 Finite-amplitude crossflow vortices, secondary instability and transition in the rotating-disk boundary layer. *J. Fluid Mech.* **487**, 315–343.

PIER, B. & HUERRE, P. 2001 Nonlinear self-sustained structures and fronts in spatially developing wake flows. *J. Fluid Mech.* **435**, 145–174.

PIER, B., HUERRE, P. & CHOMAZ, J.-M. 2001 Bifurcation to fully nonlinear synchronized structures in slowly varying media. *Physica* D **148**, 49–96.

PIER, B., HUERRE, P., CHOMAZ, J.-M. & COUAIRON, A. 1998 Steep nonlinear global modes in spatially developing media. *Phys. Fluids* **10**, 2433–2435.

SARIC, W. S., REED, H. L. & WHITE, E. B. 2003 Stability and transition of three-dimensional boundary layers. *Annu. Rev. Fluid Mech.* **35**, 413–440.

SIDDIQUI, M. E., MUKUND, V., SCOTT, J. & PIER, B. 2013 Experimental characterization of transition region in rotating-disk boundary layer. *Phys. Fluids* **25**, 034102.

VIAUD, B., SERRE, E. & CHOMAZ, J.-M. 2008 The elephant mode between two rotating disks. *J. Fluid Mech.* **598**, 451–464.

WILKINSON, S. P. & MALIK, M. R. 1983 Stability experiments in rotating-disk flow. *AIAA Paper* 83-1760.

WILKINSON, S. P. & MALIK, M. R. 1985 Stability experiments in the flow over a rotating disk. *AIAA J.* **23**, 588–595.